Supplementary Information for

# Quantum Simulation of Charge and Exciton Transfer in Multi-mode Models using Engineered Reservoirs

Visal So[1,*], Midhuna Duraisamy Suganthi, Mingjian Zhu, Abhishek Menon,
George Tomaras, Roman Zhuravel, Han Pu, Peter G. Wolynes,
José N. Onuchic, and Guido Pagano[1,†]

*To whom correspondence should be addressed: vs39@rice.edu
†Email: pagano@rice.edu

## CONTENTS

## I. SYSTEM CALIBRATION

As described in the main text, we have full control over the system parameters and the properties of the reservoirs. Prior to realizing the two-mode LVCM dynamics with the twelve laser tones, we independently calibrate each term of the Hamiltonian and the motional cooling of each vibrational mode using their corresponding laser configurations, following the procedure detailed in Ref. [1], with additional steps for the drives associated with the second vibrational mode. The following table lists out the values of the system parameters and motional cooling rates used to realize the LVCM dynamics in the main text:

| **Reported data** | **Trapped-ion parameters [$2\pi\times$ kHz]** | | | | | | | |
|---|---|---|---|---|---|---|---|---|
| | $\Delta E$ | $V$ | $\omega_1$ | $g_1$ | $\gamma_1$ | $\omega_2$ | $g_2$ | $\gamma_2$ |
| Figs. 2A-B | 2–28 | 1 | 5 | 6 | 0.18 | 5 | 5.5 | 0.2 |
| Figs. 2C-D | 3–40 | 1.1 | 8 | 8.23 | 0.18 | 3 | 2.98 | 0.08 |
| Figs. 3A-B | 2–40 | 0.5 | 8 | 10.3 | 0.12 | 3 | 1.82 | 0.2 |
| Figs. 4A-B | 5–25 | 2 | 10 | 2 | 0.45 | 10 | 2.2 | 0.18 |
| Figs. 4C-D | 5–25 | 2 | 12 | 3.3 | 0.34 | 8 | 2.1 | 0.15 |

TABLE I. Trapped-ion interaction settings used for simulating the LVCM dynamics in the main text. The values of the system parameters ($\Delta E,\ V,\ \omega_1,\ g_1,\ \omega_2,\ g_2$) and vibrational dissipation rates ($\gamma_1,\ \gamma_2$) are determined by the frequency and power of the laser tones used to generate the associated ion-light interactions.

As shown in Table I, in this work, we demonstrate precise control and wide-range tunability of ion-light interactions on our quantum simulator, which allow us to explore the rich dynamics of multi-mode LVCM systems in different vibronic coupling regimes and vibrational mode degeneracy.

## II. NUMERICAL SIMULATIONS

We use a QuTiP-based Python package[2] to numerically obtain the LVCM dynamics for comparing with the experimental data and theoretical investigations. Due to experimental imperfections, we include additional decoherence processes to our simulations of Eq. (2), as follows:

$$\frac{\partial \rho}{\partial t} = -i[H,\rho] + \sum_{i=1,2}\{\gamma_i(\bar{n}_i+1)\mathcal{L}_{a_i}[\rho] + \gamma_i\bar{n}_i\mathcal{L}_{a_i^\dagger}[\rho]\} + \gamma_z\mathcal{L}_{\sigma_y}[\rho] + \sum_{i=1,2}\gamma_{im}\mathcal{L}_{c_{im}}[\rho], \quad \text{(S1)}$$

where the jump operator $\sigma_y$ and its corresponding rate $\gamma_z$ account for spin dephasing induced by laser power fluctuations in the rotated spin basis ($z \leftrightarrow y$), while the jump operators $c_{im} = a_i a_i^\dagger + a_i^\dagger a_i$ and their corresponding rates $\gamma_{im}$ consider the motional dephasing of the radial tilt modes due to trap frequency fluctuations[1,3]. From the comparison between the numerical calculations and experimental data, we obtain $\gamma_z/2\pi = 7$ Hz and $\gamma_{im}/2\pi = 20$ Hz for all cases.

## III. PERTURBATIVE ANALYSIS

### A. Weak electronic coupling

Throughout the main text, we focus our investigation of the two-mode CT process in the strong electronic coupling regime ($|V| \sim \lambda_i/4$), where there is no analytical description for the rate of the transfer dynamics. However, in the weak electronic coupling regime, where $|V| \ll \lambda_i/4$, the eigenstates of the two-mode LVCM can be approximated to the two-dimensional uncoupled donor and acceptor vibronic states, where we treat the electronic coupling term $V\sigma_x$ as a perturbation to the uncoupled system, described by $H - V\sigma_x$ with $g_i \gtrsim \omega_i$. In this case, the transfer rates are given by the Fermi's golden rule (FGR) for the transitions between the donor and acceptor vibronic states, as follows[1,4–7]:

$$k_T = 2\pi|V|^2 \sum_{\substack{n_{1-},n_{1+}\\ n_{2-},n_{2+}}} p_{n_{1-}} p_{n_{2-}} \mathrm{FC}_{\substack{n_{1-},n_{1+}\\ n_{2-},n_{2+}}} \mathrm{L}(E_{DA},\gamma_{\text{eff}}), \quad \text{(S2)}$$

where $\mathrm{FC}_{\substack{n_{1-},n_{1+}\\ n_{2-},n_{2+}}} = |\langle n_{1-}|n_{1+}\rangle \langle n_{2-}|n_{2+}\rangle|^2$ is the convolution of the Franck-Condon factors of the two vibrational modes, which describes the total two-dimensional overlap between the displaced Fock wavefunctions, and $p_{n_{i-}}$ is the initial phonon population of the vibrational mode $i$ in the donor state. Here, we account for the dissipation of the vibrational modes by including a Lorentzian energy distribution to the resonances at $E_{DA} \equiv E_{D,n_{1-},n_{2-}} - E_{A,n_{1+},n_{2+}} = \Delta E$, the difference between the eigenenergies of the uncoupled donor $|D\rangle \otimes |n_{1-}\rangle \otimes |n_{2-}\rangle$ and acceptor $|A\rangle \otimes |n_{1+}\rangle \otimes |n_{2+}\rangle$ vibronic states. The line-broadening profile takes the form:

$$\mathrm{L}(E_0,\gamma) = \frac{\gamma/2\pi}{E_0^2 + \gamma^2/4}. \tag{S3}$$

The effective spectral width of the broadening is $\gamma_{\text{eff}} = C_1\gamma_1 + C_2\gamma_2$, where the vibrational mode $i$ is independently subjected to the dissipation rate $\gamma_i$ with $\gamma_i \gtrsim |V|$, and $C_i$ corresponds to its correction factor, which is explained below. The effective broadening arises from the convolution of two Lorentzian distributions of widths $C_1\gamma_1$ and $C_2\gamma_2$. This description can be extended to the perturbative CT systems with a higher number of vibrational modes ($i > 2$).

Regarding the width of the line broadening associated with the vibrational dissipation in perturbative CT systems, we numerically find that it depends not only on the dissipation rate $\gamma_i$ but also on the displacement given by $g_i/\omega_i$. This dependence is related to the fact that the Lindbladian eigenvalues are diagonal in the non-displaced Fock basis, and not in the eigenbasis of the vibronic system, which causes the collapse operator to act on both the donor and acceptor vibronic states[8]. To demonstrate this finding, we revisit the single-mode CT case with a vibrational energy $\omega$ and a vibronic coupling $g$ subject to vibrational dissipation at a rate $\gamma$. The effective full width at half maximum of the Lorentzian broadening is presumed to be $\gamma_{\text{eff}} = C\gamma$. As shown in Fig. S1A, we empirically estimate a fixed value of the correction factor $C > 1$ for a given $g/\omega$ by comparing

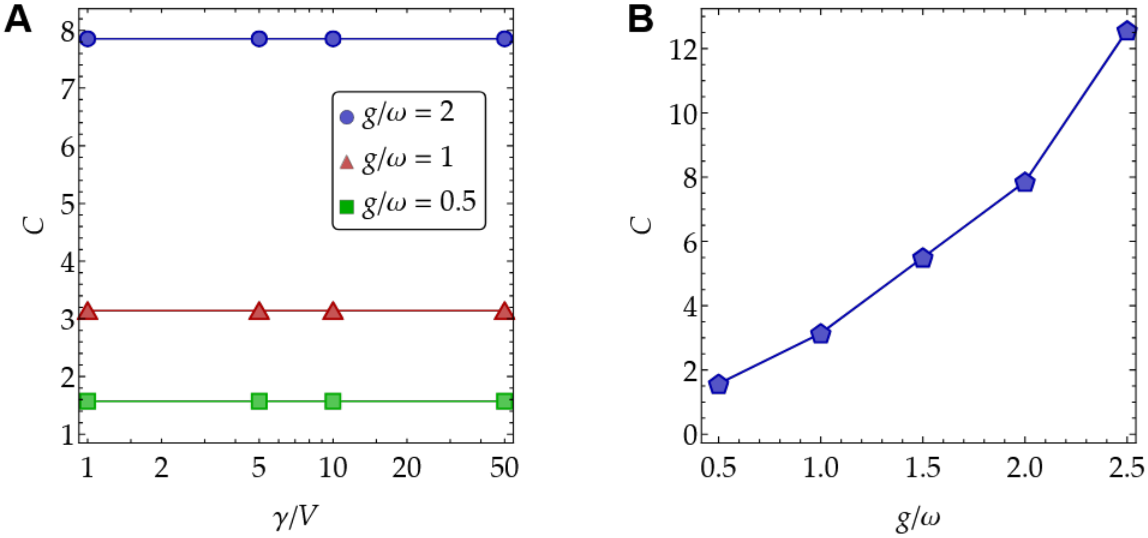

Figure S1. **Line-broadening corrections in the weak electronic coupling regime.** Empirically determined width correction factor $C$ (connecting point markers) for the single-mode CT process with $V = 0.005\omega$ and $\bar{n} = \bar{n}_0 = 0.01$, plotted as a function of (**A**) $\gamma/V$ and (**B**) $g/\omega$.

the transfer rate spectra obtained from the master equation with those from the FGR. Since $C$ is found to be independent of $\gamma$, we can deduce that the effective broadening width $\gamma_{\text{eff}}$ is linearly proportional to $\gamma$. By varying $g/\omega$ for fixed $\gamma$ and $V$ in Fig. S1B, we observe that $C$ grows as $\sim (g/\omega)^2$. For instance, when $g/\omega = 2.5$, we get $C \approx 4\pi$, the correction factor used in Ref. [6] Although $C$ seems to approach the value of 1 as $g/\omega$ goes to 0, this limit is forbidden by the perturbation criterion of the regime, which requires $|V| \ll \lambda/4$. However, $C = 1$ is appropriate for the analysis of the perturbative VAET dynamics in Supplementary Information III B, where $g$ is the perturbation to the uncoupled vibronic system, whose eigenstates are the products of the electronic states and the non-displaced Fock states.

It is also worth noting that we have used the definition in Eq. (3) for the transfer rate to capture both the time it takes for the system to equilibrate and the steady-state population of the dynamics throughout the main text for our non-perturbative studies. As pointed out in Refs. [6, 9], given an exponentially decaying dynamics with no remaining population in the initial state, the transfer

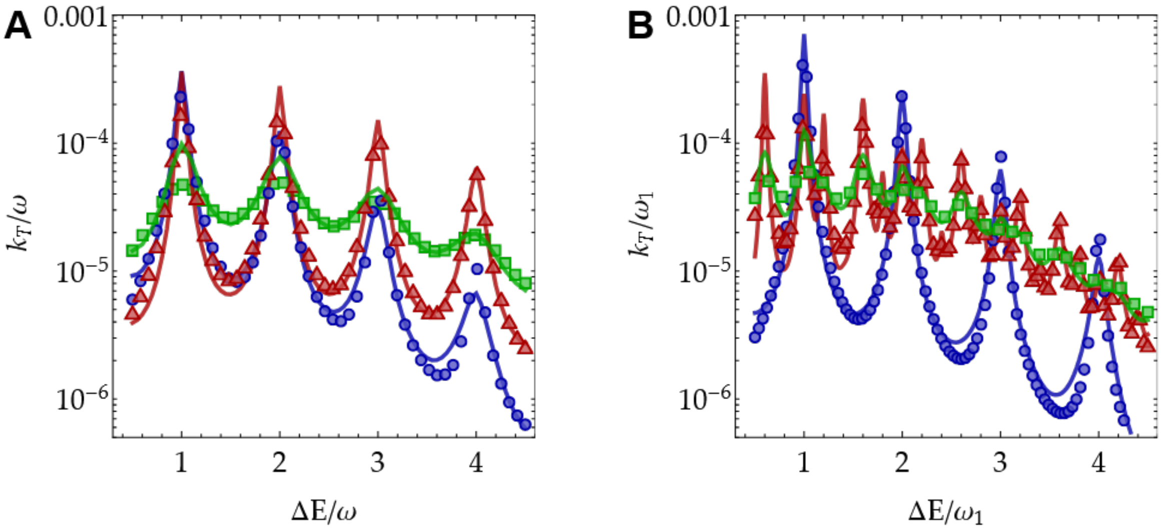

Figure S2. **Transfer rates in the weak electronic coupling regime.** (**A**) Transfer rate spectra for the degenerate two-mode CT case ($\omega_1 = \omega_2 \equiv \omega$) with $(V, g_1, g_2) = (0.005, 1, 1)\omega$ and $\bar{n}_{0,i} = \bar{n}_i = 0.01$. Red and green data correspond to $(\gamma_1, \gamma_2) = (0.04, 0.01)\omega$ and $(0.05, 0.15)\omega$, respectively. Blue data are the numerical results of the single-mode CT process, where $\omega_2 = g_2 = \gamma_2 = 0$ and $\gamma_1 \equiv \gamma = 0.05\omega$. (**B**) Transfer rate spectra for the non-degenerate two-mode CT case ($\omega_1 > \omega_2$) with $(V, g_1, g_2, \omega_2) = (0.005, 1, 1, 0.6)\omega_1$. Similarly, red and green data correspond to $(\gamma_1, \gamma_2) = (0.025, 0.005)\omega_1$ and $(0.025, 0.075)\omega_1$, respectively. Blue data are the numerical results of the single-mode CT process, where $\omega_2 = g_2 = \gamma_2 = 0$ and $\gamma_1 \equiv \gamma = 0.025\omega_1$. The solid curves show the transfer rates obtained from the exponential fits of the master equation dynamics, while the point markers are their corresponding FGR predictions from Eq. (S2).

rate calculated by Eq. (3) converges to the inverse of the time constant at sufficiently large $t_{\text{sim}}$. However, when the population transfer is not complete ($P_D^{\text{SS}} \equiv P_D(t \to \infty) > 0$), the absolute values of the rates extracted from Eq. (3) differ from those obtained via the exponential fits despite retaining the same qualitative behaviors in the transfer rate spectra. Therefore, when comparing the transfer rates of the perturbative dynamics given by the master equation with the FGR predictions, it is more accurate to use the inverse time constants from the exponential fits rather than the rates obtained from Eq. (3).

By considering these effects in our analysis, we observe that the FGR calculations agree well with the numerical results of the master equation in Eq. (2) for weak electronic couplings ($V = 0.02 \times \lambda_i/4$), as shown in Fig. S2. Despite the overall increase in the energetically allowed transfer robustness, there are some subtle differences in the transfer behaviors between the degenerate ($\omega_1 = \omega_2 \equiv \omega$) and non-degenerate ($\omega_1 > \omega_2$) cases when compared to their single-mode ($\omega_2 = g_2 = \gamma_2 = 0$) counterparts. Thus, we shall discuss their features separately:

**Degenerate case** ($\omega_1 = \omega_2 \equiv \omega$) - As shown by the red and blue curves in Fig. S2A, the transfer rates of the two-mode system are lower to those of the single-mode system around $\Delta E = \omega$, and they become larger at higher resonances ($\Delta E = m\omega, m \in \mathbb{N}, m > 1$) for $\gamma_1 + \gamma_2 = \gamma$. This can be understood by comparing the FGR formula of the single-mode and two-mode cases. At a low temperature ($\bar{n}_i \sim 0.01$), the initial population in both cases dominantly occupies the ground level of the donor well. For $\Delta E = m\omega, m \in \mathbb{N}$, the transfer rates are proportional to the wavefunction overlaps between the donor and acceptor states, given by $\mathrm{FC}_{2\mathrm{M}} \approx \sum_{k_1=0}^{m} \sum_{k_2=0}^{m} \delta_{k_1+k_2,m} |\langle 0_- | k_{1+} \rangle|^2 |\langle 0_- | k_{2+} \rangle|^2$ in the degenerate two-mode case and $\mathrm{FC}_{1\mathrm{M}} \approx |\langle 0_- | m_+ \rangle|^2$ in the single-mode case, where we suppose $p_{n_{i-}} \equiv p_{n_-} \approx p_{0_-} \approx 1$ and $|\langle n_{i-} | n_{i+} \rangle| \equiv |\langle n_- | n_+ \rangle| \leq 1$ for simplicity. Intuitively, the vibrational modes of the two-dimensional donor well can "share" the energy difference, increasing the likelihood of transitions to higher excited states of the two-dimensional acceptor well (for $m > 1$) despite the lessened individual couplings from the smaller wavefunction overlaps as compared to the single-mode case. For example, for a well separation of $g_i/\omega_i = 1$ between the donor and acceptor energy surfaces, the Franck-Condon factors of the two systems decrease with increasing $\Delta E = m\omega$ as follows: $\mathrm{FC}_{2\mathrm{M}} = \{0.271, 0.271, 0.180, 0.124\}$ and $\mathrm{FC}_{1\mathrm{M}} = \{0.368, 0.184, 0.061, 0.015\}$ for $m = \{1, 2, 3, 4\}$, which explains the comparative features of the red and blue data points in Fig. S2A.

However, for increasing width $\gamma$, the transfer dependence on $\Delta E$ can be diminished at the expense of the transfer rates at resonances. As shown in the green curve of Fig. S2A, when we increase the dissipation rate on the slow mode, the widths of the two-mode transfer resonances grow despite the lowered peak values, which increases the transition probabilities for off-resonant processes, thus making excitation transfer more robust to the energy offset in the donor-acceptor system.

**Non-degenerate case** $(\omega_1 > \omega_2)$ - The additional resonances, provided by the slow mode, can also increase the transfer robustness to $\Delta E$ (see Fig. S2B). Extra broadening of the resonances from increased $\gamma_{\text{eff}}$ can further enhance this robustness. Meanwhile, the transfer rates at resonances associated with the fast mode ($\Delta E = m\omega_1, m \in \mathbb{N}$) are evidently reduced compared to the single-mode system, differently from the degenerate case. This decrease can be explained by the significantly lowered overlaps of the wavefunctions $\left(\sum_{\substack{n_{1-},n_{1+}\\ n_{2-},n_{2+}}} \mathrm{FC}_{\substack{n_{1-},n_{1+}\\ n_{2-},n_{2+}}} \ll \sum_{n_-,n_+} \mathrm{FC}_{n_-,n_+}\right)$ due to the mismatch of the resonances between those associated with the fast vibrational mode and those provided by the slow vibrational modes ($\Delta E = m\omega_1 \neq m\omega_2$).

### B. Weak vibronic coupling (VAET)

To gain insights into the VAET regime, we shall employ a similar perturbative analysis of the two-mode model in the weak vibronic coupling regime $(g_j \ll \omega_j)$[10,11]. The unperturbed system is now the uncoupled, non-displaced vibronic system, described by:

$$H_{\text{2M,unc}}^{\text{VAET}} = \frac{\Delta E}{2}\sigma_z + V\sigma_x + \sum_{j=1}^{2} \omega_j a_j^\dagger a_j. \tag{S4}$$

The eigenstates of this system are given by:

$$|e_\pm,n_1,n_2\rangle = \left( \pm \frac{\epsilon \pm \Delta E/2}{\sqrt{2\epsilon(\epsilon \pm \Delta E/2)}} |\uparrow\rangle + \frac{V}{\sqrt{2\epsilon(\epsilon \pm \Delta E/2)}} |\downarrow\rangle \right) \otimes |n_1\rangle \otimes |n_2\rangle\,, \tag{S5}$$

which correspond to the eigenenergies $E_{e\pm,n_1,n_2} = \pm\epsilon + n_1\omega_1 + n_2\omega_2$, where $\epsilon \equiv \sqrt{\left(\frac{\Delta E}{2}\right)^2 + V^2}$, and $n_j \in \mathbb{N}$. Without the vibrational displacements being parts of the uncoupled vibronic system, the concept of state-dependent potential energy landscape does not apply here, and $H^{\mathrm{VAET}}_{\mathrm{Int}} = \sum_{j=1}^{2} \frac{g_j}{2}\sigma_z(a_j + a_j^\dagger)$ rather acts as a perturbation that induces transitions between the states with ladder-like energy levels. By transforming into the eigenstate basis defined in Eq. (S5), the vibronic perturbation can be written as:

$$H^{\mathrm{VAET}}_{\mathrm{Int},e} = \sum_{j=1}^{2} \frac{g_j}{2\epsilon}\left(\frac{\Delta E}{2}\tilde{\sigma}_z - V\tilde{\sigma}_x\right)(a_j + a_j^\dagger), \tag{S6}$$

where $\tilde{\sigma}_{x,z}$ are the Pauli operators in the eigenstate basis. From the first-order perturbation theory, single-phonon exchange processes are allowed, and the transfer rates are given by the first-order transition probability amplitude $C_T^{(1)}$ and the final density of states $\rho_F(E_I)$:

$$\begin{aligned} k_T^{(1)} &= 2\pi \left|C_T^{(1)}\right|^2 \rho_F(E_I) \\ &= 2\pi \left|\frac{V}{2\epsilon}\right|^2 \sum_{\substack{n_{1I},n_{1F}\\ n_{2I},n_{2F}}} p_{n_{1I}} p_{n_{2I}} \sum_{j=1}^{2} |g_j|^2 \delta_{n_{kF},n_{kI}} \\ &\quad \times \left[n_{jI}\delta_{n_{jF},n_{jI}-1} + (n_{jI}+1)\delta_{n_{jF},n_{jI}+1}\right] \mathrm{L}(E_{IF},\gamma_j), \end{aligned} \tag{S7}$$

where index $k \neq j$, specifically $(j,k)$ can only be either $(1,2)$ or $(2,1)$, and $E_{IF} \equiv E_{e+,n_{1I},n_{2I}} - E_{e-,n_{1F},n_{2F}} = 2\epsilon + (n_{1I} - n_{1F})\omega_1 + (n_{2I} - n_{2F})\omega_2$ is the energy difference between the initial $|e_+, n_{1I}, n_{2I}\rangle$ and final $|e_-, n_{1F}, n_{2F}\rangle$ eigenstates. The allowed transfers in Eq. (S7) describe the processes in which the vibronic system exchanges single-phonon energy with the environment to enable the excitation transfer[10,12].

In contrast to the CT regime, where the collapse operators—diagonal in the Fock basis—act on displaced Fock states, the dissipation in VAET applies directly to the vibrational degrees of free-

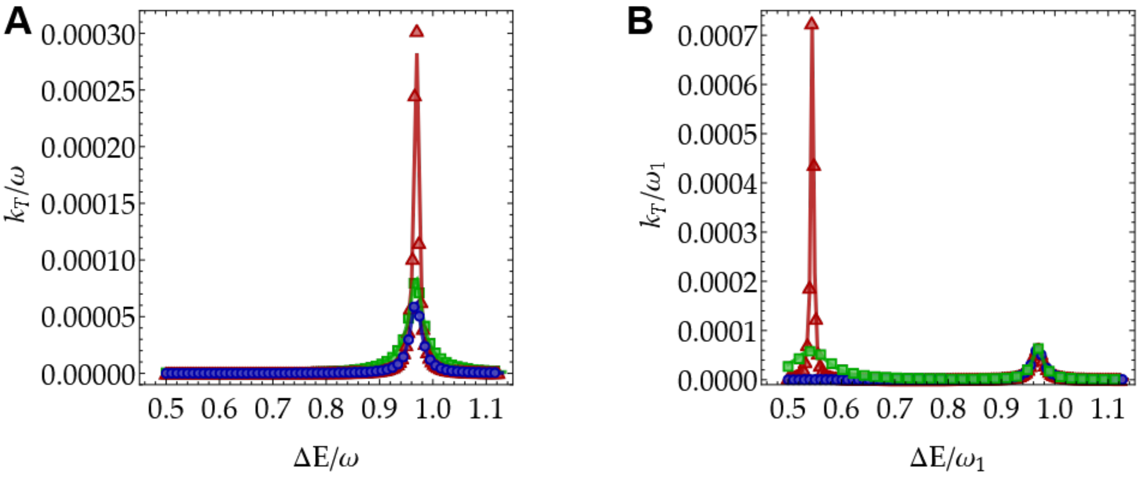

Figure S3. **Transfer rates in the weak vibronic coupling regime associated with VAET.** (**A**) Transfer rate spectra for the degenerate case ($\omega_1 = \omega_2 \equiv \omega$) with $(V, g_1, g_2) = (0.125, 0.005, 0.005)\omega$ and $\bar{n}_{0,i} = \bar{n}_i = 0.01$. Red and green data correspond to $(\gamma_1, \gamma_2) = (0.020, 0.005)\omega$ and $(0.025, 0.075)\omega$, respectively. Blue data are the numerical results of the single-mode VAET case, where $\omega_2 = g_2 = \gamma_2 = 0$ and $\gamma_1 \equiv \gamma = 0.025\omega$. (**B**) Transfer rate spectra for the non-degenerate case ($\omega_1 > \omega_2$) with $(V, g_1, g_2, \omega_2) = (0.125, 0.005, 0.005, 0.6)\omega_1$. Similarly, red and green data correspond to $(\gamma_1, \gamma_2) = (0.025, 0.005)\omega_1$ and $(0.025, 0.075)\omega_1$, respectively. Blue data are the same as in (A). The solid curves show the transfer rates obtained from the exponential fits of the master equation dynamics, while the point markers are their corresponding first-order FGR predictions from Eq. (S7).

dom of the eigenstates (non-displaced Fock states), and thus the associated line broadening does not require any correction factor ($C = 1$). More importantly, since the first-order processes in the VAET regime only require an excitation from one of the two available vibrational modes in the two-mode system, the spectral width of the transfer resonance is exactly equal to the dissipation rate of the relevant mode, analogous to a two-level system undergoing dissipation[13]. Similarly, the number of participating phonons and their corresponding dissipation rates determine the spectral widths of the multi-phonon exchange resonances through the convolution of the Lorentzian distributions associated with the relevant vibrational levels. This is different from the broadening in CT, where the effective linewidth is independent of the amount of involved vibrational quanta and is common for all the resonances that transfer excitation from the donor to the acceptor two-dimensional potential energy wells.

Moreover, Eq. (S7) suggests that there is an asymmetry of the transfer rates between the resonances associated with exothermic ($E_{IF} > 0$) and endothermic ($E_{IF} < 0$) transfers at low temperatures, also observed in Ref. [10]. However, in the very low-temperature regime ($n_{jI} \approx 0$), we can further simplify the expression by considering only the terms associated with the phonon-gain resonances (exothermic transfers). Thus, the formula for the single-phonon transfer rates is reduced to:

$$k_T^{(1)} = 2\pi \left| \frac{V}{2\epsilon} \right|^2 \sum_{\substack{n_{1I}, n_{1F} \\ n_{2I}, n_{2F}}} p_{n_{1I}} p_{n_{2I}} \sum_{j=1}^{2} |g_j|^2 \delta_{n_{kF}, n_{kI}} (n_{jI} + 1) \delta_{n_{jF}, n_{jI}+1} \mathrm{L}(E_{IF}, \gamma_j). \tag{S8}$$

In Fig. S3, we plot the transfer rates given by the time constants of the master equation dynamics (solid curves) and the first-order FGR calculations (point markers). The blue data corresponds to the single-mode system, whereas the red and green data include the additional vibrational mode with weak and strong dissipation, respectively. Unlike CT, where the introduction of the second mode directly modifies the wavefunction overlaps and, in turn, the effective coupling strength between the donor and acceptor sites, the contributions of the second mode to the transfer rates in the VAET regime are different. Since the FGR predictions in Eqs. (S7) and (S8) are probabilistically additive for the allowed transitions, the presence of the additional mode can increase the overall transfer rates of the system when the two vibrational modes are degenerate, as shown in Fig. S3A. However, when the two modes have sufficiently different frequencies, a new transfer resonance enabled by the second mode emerges but has a negligible effect on the transfer rate associated with the first-mode resonance, which is equivalent to that of the single-mode resonance (see Fig. S3B). Similar to CT, in the VAET regime, the dissipation rate of the second vibrational mode controls the trade-off between the transfer rate enhancement and increased robustness.

Although the total transfer rates are given by $k_T = 2\pi \left| \sum_{m=1}^{\infty} C_T^{(m)} \right|^2 \rho_F(E_I)$, the complexity of the analytical expression of the transfer rates grows with the order of perturbation $m$. Since the effects of higher-order contributions are minimal due to the suppressive nature of perturbative calculations, it is therefore sufficient to consider only the numerical results of the first-order contributions for our discussion above ($k_T \approx k_T^{(1)}$). However, it is worth noting that higher-order perturbations can give rise to energy-exchange processes involving more than one phonon excitation. For instance, the second-order contributions allow two-phonon exchange processes, whose transfer rates for $|2\epsilon| > 0$ are described by:

$$
\begin{aligned}
k_T^{(2)} &= 2\pi \left| C_T^{(2)} \right|^2 \rho_F(E_I) \\
&= 2\pi \sum_{\substack{n_{1I},n_{1F} \\ n_{2I},n_{2F}}} p_{n_{1I}} p_{n_{2I}} \left| \frac{V \Delta E}{\epsilon} \right|^2 \\
&\quad \times \left\{ \sum_{j=1}^{2} \left| \frac{g_j}{2} \right|^4 \delta_{n_{kF},n_{kI}} \left[ \frac{n_{jI}(n_{jI}-1)}{(2\epsilon+\omega_j)^2 \omega_j^2} \delta_{n_{jF},n_{jI}-2} + \frac{(n_{jI}+1)(n_{jI}+2)}{(2\epsilon-\omega_j)^2 \omega_j^2} \delta_{n_{jF},n_{jI}+2} \right] \mathrm{L}(E_{IF}, 2\gamma_j) \right. \\
&\quad + \left| \frac{g_1 g_2}{4} \right|^2 \left[ (n_{1I}+1)(n_{2I}+1) \left( \frac{(2\epsilon-\omega_1)\omega_1 + (2\epsilon-\omega_2)\omega_2}{(2\epsilon-\omega_1)\omega_1(2\epsilon-\omega_2)\omega_2} \right)^2 \delta_{n_{1F},n_{1I}+1} \delta_{n_{2F},n_{2I}+1} \right. \\
&\quad + (n_{1I}+1) n_{2I} \left( \frac{(2\epsilon-\omega_1)\omega_1 - (2\epsilon+\omega_2)\omega_2}{(2\epsilon-\omega_1)\omega_1(2\epsilon+\omega_2)\omega_2} \right)^2 \delta_{n_{1F},n_{1I}+1} \delta_{n_{2F},n_{2I}-1} \\
&\quad + n_{1I}(n_{2I}+1) \left( \frac{(2\epsilon-\omega_2)\omega_2 - (2\epsilon+\omega_1)\omega_1}{(2\epsilon+\omega_1)\omega_1(2\epsilon-\omega_2)\omega_2} \right)^2 \delta_{n_{1F},n_{1I}-1} \delta_{n_{2F},n_{2I}+1} \\
&\quad \left. \left. + n_{1I} n_{2I} \left( \frac{(2\epsilon+\omega_1)\omega_1 + (2\epsilon+\omega_2)\omega_2}{(2\epsilon+\omega_1)\omega_1(2\epsilon+\omega_2)\omega_2} \right)^2 \delta_{n_{1F},n_{1I}-1} \delta_{n_{2F},n_{2I}-1} \right] \mathrm{L}(E_{IF}, \gamma_1+\gamma_2) \right\} .
\end{aligned}
\tag{S9}
$$

For completeness, in the expression above, we include the negative energy input resonances ($2\epsilon < 0$) even if they are suppressed in the case of low temperatures investigated in this work. There are two classes of two-phonon exchange processes here: single-mode exchange and double-mode exchange[11]. In the former type, two phonons from a specific vibrational mode participate in the exchange, while the latter class consists of processes in which one phonon from each mode contributes to the two-phonon-assisted processes.

Another difference between the CT and VAET regimes is related to high-$\Delta E$ transfers. In the CT regime, both the initial temperature and displacement-dependent Franck-Condon factors determine whether highly excited processes are allowed. However, in the VAET regime, multi-phonon exchange processes are always suppressed due to the progressively decreasing coupling strengths with respect to the orders of perturbative calculations.

Alternatively to the perturbation analysis, we can use the non-interacting blip approximation to track the spin dynamics of VAET, as described below in Supplementary Information IV. Despite its closed-form formula, its evaluation heavily relies on the complexity of the spectral density function describing the environmental influences on the pure spin systems.

## IV. SOLUTION FOR VAET UNDER NIBA

In this section, we derive a closed-form solution for open-system VAET under the non-interacting blip approximation (NIBA) by considering the following spin-boson model[4,14]:

$$H_{\mathrm{sb}} = \frac{\Delta E}{2}\sigma_z + V\sigma_x + \sum_{k=1}^{\infty}\frac{\lambda_k}{2}\sigma_z\left(a_k^\dagger + a_k\right) + \sum_{k=1}^{\infty}\omega_k a_k^\dagger a_k, \tag{S10}$$

where, in the continuum limit, the couplings between the spin and each bosonic mode and the frequencies of the infinite bosonic bath are characterized by the spectral density $J(\omega) = \pi\sum_k \lambda_k^2\delta(\omega-\omega_k)$. It has also been shown in Ref. [15] that if the spectral density takes the form:

$$J(\omega) = \sum_{i=1}^{2} g_i^2\left(\frac{\gamma_i}{\gamma_i^2 + (\omega_i - \omega_{im})^2} - \frac{\gamma_i}{\gamma_i^2 + (\omega_i + \omega_{im})^2}\right), \tag{S11}$$

with $\gamma_i,\ \omega_i$, and $g_i$ defined in the main text and $\omega_{im} = \sqrt{\omega_i^2 - \gamma_i^2}$, the spin dynamics generated by the spin-boson model in Eq. (S10) is equivalent to that generated by the dissipative LVCM system described by Eq. (2) in the main text under the conditions $\gamma_i \ll \omega_{im}$ and $\gamma_i \ll k_B T_i$ for $k_B T_i \equiv k_B T = 1/\beta$ (the same temperature for all bosonic bath modes).

Given the above spectral density function, the coupling strength between the spin and each bosonic bath mode is characterized by $g_i$, which is small when compared to $\omega_i$, $E$, and $V$ in the VAET regime. Therefore, it is appropriate to apply the weak-coupling approximation with NIBA[4,14]. The vibronic coupling terms in Eq. (S10) can then be canceled out by applying a unitary transformation $U = \exp\left(\sum_k \alpha_k (a_k^\dagger - a_k)\right)$ with $\alpha_k = -\frac{1}{2}\frac{\lambda_k}{\omega_k}\sigma_z$, such that the transformed Hamiltonian becomes:

$$U^\dagger H U = \frac{\Delta E}{2}\sigma_z + V\left(\sigma^+ e^{-iB} + \sigma^- \sigma^{iB}\right) + \sum_k \omega_k a_k^\dagger a_k, \tag{S12}$$

where the operator $B = i\sigma_z \sum_k \frac{\lambda_k}{\omega_k}(a_k^\dagger - a_k)$. We then follow the procedure in the Supplementary Information of Ref. [16] and write down the spin equations of motion in the Heisenberg picture:

$$\begin{aligned} \partial_t \sigma_{z,H} &= i2V(\sigma_H^- e^{iB(t)} - \sigma_H^+ e^{-iB(t)}), \\ \partial_t \sigma_H^+ &= i\Delta E \sigma_H^+ - iV\sigma_{z,H} e^{iB(t)}, \end{aligned} \tag{S13}$$

where $\sigma_{z,H}$ and $\sigma_H^+$ are the time-dependent Pauli operators in the Heisenberg picture. We can solve for $\sigma_H^+$ in terms of $\sigma_{z,H}$ from the second equation and substitute the solution into the first equation. By taking the expectation value, we get:

$$\partial_t \langle \sigma_z \rangle = -2V^2 \int_0^t ds \langle \sigma_z \rangle (s)\, e^{-iE(t-s)} \langle e^{-iB(s)} e^{iB(t)} \rangle + \text{h.c.} \tag{S14}$$

With NIBA, we suppose that the bath evolution is decoupled from that of the spin such that the expectation value $\langle e^{-iB(s)} e^{iB(t)} \rangle$ can approximately be calculated by considering the evolution of the bosonic modes under the free bath Hamiltonian $\sum_k \omega_k a_k^\dagger a_k$. Assuming each bath mode is at equilibrium with a temperature $k_B T$ and utilizing the second-order cumulant expansion $\langle \exp X \rangle \to \exp \langle X + \frac{1}{2}\mathrm{Var}\,(X) \rangle$, we have:

$$\langle e^{-iB(s)} e^{iB(t)} \rangle = \exp\left(-iQ_1\left(t-s\right)\right) \exp\left(Q_2\left(t-s\right)\right), \tag{S15}$$

where

$$\begin{aligned} Q_1\left(\tau\right) &= \frac{1}{\pi}\int_{-\infty}^{\infty} d\omega J(\omega)\sin\left(\omega\tau\right)/\omega^2, \\ Q_2\left(\tau\right) &= \frac{1}{\pi}\int_{-\infty}^{\infty} d\omega J(\omega)\left(\cos\left(\omega\tau\right)-1\right)\coth\left(\beta\omega/2\right)/\omega^2. \end{aligned} \tag{S16}$$

By inserting Eq. (S15) into Eq. (S14), the equation of motion for $\langle \sigma_z \rangle$ takes the form of a convolution with a kernel function $f(\tau)$:

$$\begin{aligned} \partial_t \left\langle \sigma_z \right\rangle &= \int_0^t ds f\left(t-s\right)\left\langle \sigma_z \right\rangle\left(s\right), \\ f\left(\tau\right) &= -4V^2\cos\left(Q_1\left(\tau\right)-\Delta E\tau\right) e^{Q_2(\tau)}, \end{aligned} \tag{S17}$$

which can be formally solved using the Laplace transform:

$$\left\langle \sigma_z \right\rangle\left(t\right) = \mathcal{L}^{-1}\left[\frac{\langle \sigma_z \rangle (t=0)}{\zeta - \widetilde{f}(\zeta)}\right], \tag{S18}$$

where $\tilde{f}(\zeta) = \mathcal{L}[f(\tau)]$ is the Laplace transform of the kernel function $f$.

## V. INTERFERENCE EFFECTS IN TWO-MODE VAET

To better understand the interference effects in two-mode VAET systems leading to the enhancement at $\omega_1+\omega_2$ resonance in the main text, we examine the zero-temperature case ($p_{n_{jI}=0} = 1,\ p_{n_{jI}\neq 0} = 0$) in Eq. (S10), which gives the rates of transfer between the eigenstates in Eq. S5 for $\Delta E = \sqrt{(\omega_1+\omega_2)^2 - V^2} \equiv E_{\text{dual}}$ and $\Delta E = \sqrt{(2\omega_i)^2 - V^2} \equiv E^i_{\text{single}}$:

$$k_T^{(2)}(E_{\text{dual}}) = 2\pi \left[ \frac{g_1 g_2 V E_{\text{dual}}}{(\omega_1+\omega_2)^2} \left( \frac{1}{\omega_1} + \frac{1}{\omega_2} \right) \right]^2 \mathrm{L}(E_{\text{dual}}, \gamma_1+\gamma_2), \tag{S19}$$

$$k_T^{(2)}(E^i_{\text{single}}) = 2\pi \left[ \frac{g_i^2 V E^i_{\text{single}}}{(2\omega_i)^2} \frac{\sqrt{2}}{\omega_i} \right]^2 \mathrm{L}(E^i_{\text{single}}, 2\gamma_i), \tag{S20}$$

respectively. When $\omega_1 = \omega_2 \equiv \omega$, $g_1 = g_2 \equiv g$, and $\gamma_1 = \gamma_2 \equiv \gamma$, Eqs. (S19) and (S20) give $k_T^{(2)}(E_{\text{dual}}) = 2 \times k_T^{(2)}(E^i_{\text{single}})$, explaining the enhancement at the second resonance of the degenerate two-mode VAET compared to its single-mode counterpart, as observed in Fig. 4A. Similarly, for $\omega_1 > \omega_2$ and $g_i \ll \omega_i$, we get $k_T^{(2)}(E_{\text{dual}}) > k_T^{(2)}(E^i_{\text{single}})$, as observed in Fig. 4C.

## VI. BEYOND TWO-MODE LVCM

Here, we show how the conclusions of our work on the two-mode models can be straightforwardly extended to the three-mode models and presumably to multi-mode models with $i > 3$ with Figs. S4 and S5. Similar to the degenerate two-mode CT process, the presence of the additional vibrational mode in the degenerate three-mode CT case increases the phase-space volume of the hybridized energy surfaces (now three-dimensional), which leads to a wider $\Delta E$ region with monotonically increasing transfer rates and sharper peaks at high-$\Delta E$ ($\geq 5\omega$) resonances corresponding to the release of the initially trapped population in the three-dimensional upper adiabatic states (see Fig. S4A). Meanwhile, as shown in Fig. S4B, when the vibrational energies are not all

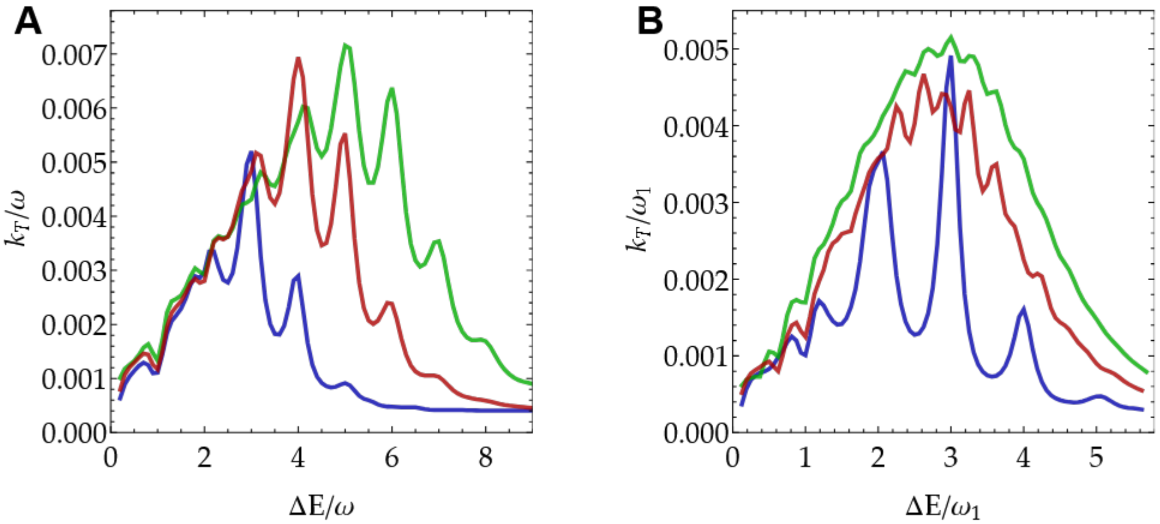

Figure S4. **Transfer rates for different numbers of vibrational modes involved in CT.** (**A**) Transfer rate spectra for the degenerate case ($\omega_1 = \omega_2 = \omega_3 \equiv \omega$) with $(V, g_i, \gamma_i) = (0.2, 1, 0.02)\omega$ for $i = 1, 2$, and 3. (**B**) Transfer rate spectra for the non-degenerate case ($\omega_1 > \omega_2 > \omega_3$) with $(V, g_1, \gamma_1, \omega_2, \omega_3) = (0.125, 1, 0.025, 0.625, 0.375)\omega_1$, $(g_2, \gamma_2) = (1, 0.020)\omega_2$, and $(g_3, \gamma_3) = (1, 0.033)\omega_3$. In both cases, the solid curves represent the transfer rates calculated from Eq. (2) using the definition in Eq. (3) with the same additional decoherences used in the main text. The blue, red, and green curves are the numerical results of the CT systems with one vibrational mode ($i = 1$ only), two vibrational modes ($i = 1$ and 2), and three vibrational modes ($i = 1, 2$, and 3), respectively.

equal, the transfer rate spectrum features a smooth transfer profile similar to that of two-mode CT except for the slightly increased rates, which can be explained by the additional transfer channels provided by the third vibrational mode.

In the case of three-mode VAET, the vibrational degrees of freedom provide access to three oscillator baths from which units of different phonon energies can be taken to assist the transfer and thus enable many combinative pathways for transfer resonances to occur, as shown in Fig. S5B. With degeneracy across the vibrational modes, the linear combinations of energy supply for the two-phonon resonance ($2\omega_1 = 2\omega_2 = 2\omega_3 = \omega_1 + \omega_2 = \omega_1 + \omega_3 = \omega_2 + \omega_3 = 2\omega$) drastically increase the transfer rates beyond the two-mode VAET ($2\omega_1 = 2\omega_2 = \omega_1 + \omega_2 = 2\omega$). However, compared to two-mode VAET, there is again a slight decrease in the transfer rate of the first

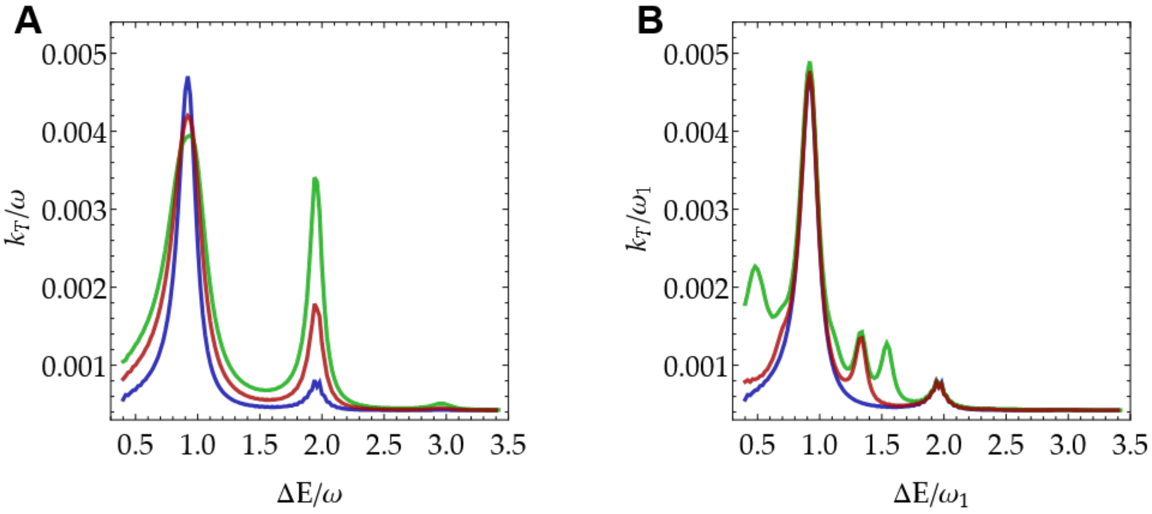

Figure S5. **Transfer rates for different numbers of vibrational modes involved in VAET.** (**A**) Transfer rate spectra for the degenerate case ($\omega_1 = \omega_2 = \omega_3 \equiv \omega$) with $(V, g_i, \gamma_i) = (0.2, 0.2, 0.04)\omega$ for $i = 1, 2$, and 3. (**B**) Transfer rate spectra for the non-degenerate case ($\omega_1 > \omega_3 > \omega_2$) with $(V, g_1, \gamma_1, \omega_2, \omega_3) = (0.2, 0.2, 0.04, 0.4, 0.6)\omega_1$, $(g_2, \gamma_2) = (0.2, 0.04)\omega_2$, and $(g_3, \gamma_3) = (0.2, 0.04)\omega_3$. In both cases, the solid curves represent the transfer rates calculated from Eq. (2) using the definition in Eq. (3) with the same additional decoherences used in the main text. The blue, red, and green curves are the numerical results of the VAET systems with one vibrational mode ($i = 1$ only), two vibrational modes ($i = 1$ and 2), and three vibrational modes ($i = 1, 2$, and 3), respectively.

resonance due to the extra broadening caused by the dissipation of the additional mode.

While the same intuition on the two-phonon resonances can be applied to the third and higher-order resonances for expected increases in the transfer rates, low-temperature VAET systems limit the transfers to few-phonon-assisted processes. As concluded in the main text, the numerical results for the three-mode systems support the generalization of the roles of mode degeneracy and vibronic coupling strength in two-mode LVCM to systems with a higher number of vibrational modes than 2 in both phenomenological regimes (CT and VAET).

## VII. VAET-CT CROSSOVER

In this section, we investigate a low-temperature single-mode LVCM system with all the system parameters fixed except for the vibronic coupling strength to understand the role of displacement in

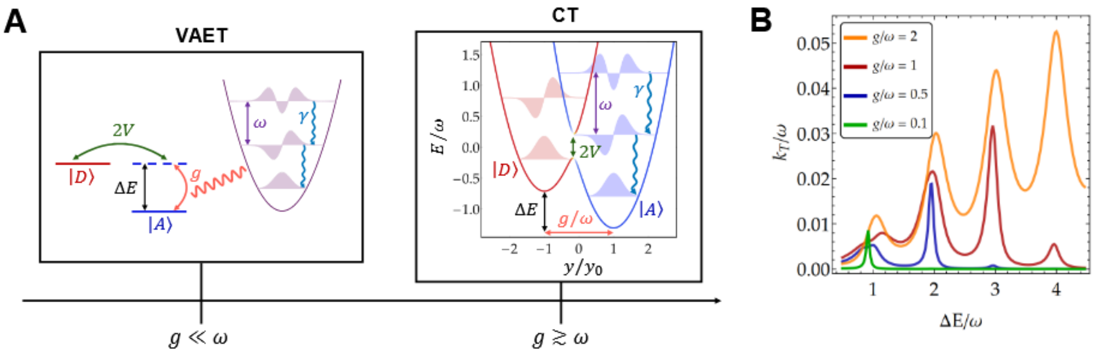

Figure S6. **VAET-CT crossover in single-mode LVCM.** (**A**) Schematic diagram illustrating the two types of transfer dynamics in single-mode models. (**B**) Transfer rate spectra with $(V, \gamma_i) = (0.2, 0.05)\omega$ at various values of $g/\omega$. All curves show the transfer rates calculated from Eq. (2) using the definition in Eq. (3).

transitioning the transfer dynamics between distinct characteristic regimes, such as VAET and CT (see Fig. S6A). For consistency, we choose the electronic coupling strength to be larger than the dissipation rate. We compare the transfer rate spectra for different values of $g/\omega = \{0.1, 0.5, 1, 2\}$ in Fig. S6B.

At small $g/\omega = 0.1$, the system undergoes VAET dynamics, showing the expected sharp transfer resonance at $\Delta E = \sqrt{\omega^2 - (2V)^2}$ from the single-phonon assisted process. As $g/\omega$ increases, the vibrational state of the system becomes effectively displaced, giving rise to non-negligible transfer rates at resonances associated with higher-order phonon-assisted processes. However, when $g \sim \omega$, the displaced LVCM system becomes an adiabatic CT system, leading to monotonically increasing transfer rates at low $\Delta E$ and sharp resonances at higher $\Delta E$ (see the results with $g/\omega = 0.5$ and 1 in Fig. S6B). From these observations, we suppose that $g \approx 0.5\omega$ is the crossover between VAET and CT. Therefore, in this work, we associate systems with $g_i/\omega_i \lesssim 0.5$ to non-perturbative VAET and systems with $g_i/\omega_i \gtrsim 1$ to non-perturbative CT, all with strong electronic coupling ($|V| \sim \lambda_i/4$).

As we further increase $g/\omega$, the system progressively evolves into the nonadiabatic regime of CT, where discernible resonance peaks are recovered across the transfer rate spectrum. Differently from VAET, these resonances occur at integer multiples of $\omega$, and the position of the strongest resonance depends on the displacement between the donor and acceptor potential energy surfaces. The two distinct regimes within CT, nonadiabatic and adiabatic transfers, are determined by the relative strengths of the electronic coupling to the reorganization energy of the system and the dissipation rate of the vibrational mode, which have been studied in Refs. [1, 6].

[1] So, V. *et al.* Trapped-ion quantum simulation of electron transfer models with tunable dissipation. *Science Advances* **10**, eads8011 (2024).

[2] Johansson, J., Nation, P. & Nori, F. Qutip 2: A python framework for the dynamics of open quantum systems. *Computer Physics Communications* **184**, 1234–1240 (2013).

[3] Flühmann, C. *et al.* Encoding a qubit in a trapped-ion mechanical oscillator. *Nature* **566**, 513–517 (2019).

[4] Leggett, A. J. *et al.* Dynamics of the dissipative two-state system. *Rev. Mod. Phys.* **59**, 1–85 (1987).

[5] Skourtis, S. S., Da Silva, A. J. R., Bialek, W. & Onuchic, J. N. New look at the primary charge separation in bacterial photosynthesis. *The Journal of Physical Chemistry* **96**, 8034–8041 (1992).

[6] Schlawin, F., Gessner, M., Buchleitner, A., Schätz, T. & Skourtis, S. S. Continuously parametrized quantum simulation of molecular electron-transfer reactions. *PRX Quantum* **2**, 010314 (2021).

[7] Onuchic, J. N. Effect of friction on electron transfer: The two reaction coordinate case. *The Journal of Chemical Physics* **86**, 3925–3943 (1987).

[8] Zhu, M., So, V., Pagano, G. & Pu, H. Dissipation-assisted steady-state entanglement engineering based on electron transfer models (2025). 2504.02101.

[9] Padilla, D. F. *et al.* Vibrationally assisted exciton transfer in open quantum systems with long-range interactions (2025). 2502.04383.

[10] Gorman, D. J. *et al.* Engineering vibrationally assisted energy transfer in a trapped-ion quantum simulator. *Phys. Rev. X* **8**, 011038 (2018).

[11] Li, Z.-Z., Ko, L., Yang, Z., Sarovar, M. & Whaley, K. B. Unraveling excitation energy transfer assisted by collective behaviors of vibrations. *New Journal of Physics* **23**, 073012 (2021).

[12] Sun, K. *et al.* Quantum simulation of spin-boson models with structured bath. *Nature Communications* **16**, 4042 (2025).

[13] Breuer, H.-P. & Petruccione, F. *The Theory of Open Quantum Systems* (Oxford University Press, 2007).

[14] Dekker, H. Noninteracting-blip approximation for a two-level system coupled to a heat bath. *Phys. Rev. A* **35**, 1436–1437 (1987).

[15] Lemmer, A. *et al.* A trapped-ion simulator for spin-boson models with structured environments. *New Journal of Physics* **20**, 073002 (2018).

[16] Kamar, N. A., Paz, D. A. & Maghrebi, M. F. Spin-boson model under dephasing: Markovian versus non-markovian dynamics. *Phys. Rev. B* **110**, 075126 (2024).